Journal of The Electrochemical Society, **151** (7) A983-A993 (2004)
0013-4651/2004/151(7)/A983/11/$7.00 © The Electrochemical Society, Inc.

Parameter Estimates for a PEMFC Cathode

Qingzhi Guo,* Vijay A. Sethuraman,* and Ralph E. White,z**

Center for Electrochemical Engineering, Department of Chemical Engineering, University of South Carolina, Columbia, South Carolina 29208, USA

Five parameters of a model of a polymer electrolyte membrane fuel cell (PEMFC) cathode (the volume fraction of gas pores in the gas diffusion layer, the volume fraction of gas pores in the catalyst layer, the exchange current density of the oxygen reduction reaction, the effective ionic conductivity of the electrolyte, and the ratio of the effective diffusion coefficient of oxygen in a flooded spherical agglomerate particle to the square of that particle radius) were determined by least-squares fitting of experimental polarization curves. The values of parameters obtained in this work indicate that ionic conduction and gas-phase transport are two processes significantly influencing the performance of PEMFC air cathodes. While ionic conduction influences cathode performance over a wide range of current densities, gas-phase transport influences cathode performance only at high current densities.

 [DOI: 10.1149/1.1747850]

Manuscript submitted October 10, 2003; revised manuscript received December 19, 2003. Available electronically May 24, 2004.

The air cathode in a polymer electrolyte membrane fuel cell (PEMFC) is the largest source of voltage loss due to limitations of ionic (proton) conduction, multicomponent gas transport, and liquid-phase O_2 diffusion.[1-3] To obtain a better understanding of these limitations, several models have been presented.[1-8] Two different pictures of the catalyst layer (CAL) have been used to model the steady-state polarization performance of a PEMFC cathode: the flooded CAL and the CAL with the existence of gas pores. The assumption of a flooded CAL was found to overestimate the product of the diffusion coefficient and the concentration of O_2 in the liquid electrolyte,[1] whereas a steady-state polarization model including gas pores in the CAL was found to be more realistic.[3,5,8]

The objective of this work was to use our previously submitted air cathode model[8] that includes gas pores in the CAL to estimate the values of the volume fraction of gas pores in the gas diffusion layer (GDL), the volume fraction of gas pores in the CAL, the exchange current density of the O_2 reduction reaction, the effective ionic conductivity of the electrolyte, and the ratio of the effective diffusion coefficient of O_2 in a flooded spherical agglomerate particle to the square of that particle radius from the experimental steady-state polarization curves of the cathode of a H_2/air PEMFC by least-squares fitting. Because the air cathode is the most important source of voltage loss in a PEMFC and the voltage loss on the H_2 anode is negligible, the experimental polarization curves of a PEMFC air cathode can be obtained from those of a H_2/air PEMFC after correcting for the voltage drop across the PEM.[1,7] In general, the model used here is similar to a model described in Jaouen *et al.*'s work.[3] The CAL is assumed to consist of many flooded spherical agglomerate particles surrounded by gas pores. As shown in Fig. 1, O_2 gas diffuses through gas pores in both the GDL and the CAL first, then dissolves into liquid water on the surface of the flooded agglomerate particles, and finally diffuses to the Pt catalyst sites or carbon surface. Protons are supplied to the Pt catalyst sites via the hydrated Nafion ionomer network in the flooded agglomerate particles. As concluded in Ref. 8, it is in the liquid form that the generated water (by the O_2 reduction reaction) is removed from the cathode GDL. Due to the hydrophobic property of the GDL, the liquid phase pressure in a cathode is larger than the gas phase pressure (capillary effect),[8] and a significant amount of liquid water is likely to be always maintained in the CAL, which makes Nafion ionomer fully hydrated. If Nafion ionomer is fully hydrated, the proton concentration is uniform in the CAL (the anion is immobile and the proton is the only ionic species in the electrolyte for charge transfer).[9] In contrast to a traditional alkaline fuel cell or a phosphoric acid fuel cell where the concentration variation of the electrolyte is important, the proton concentration in the CAL is not a variable in a PEMFC cathode model.[9] Therefore, the proton concentration was not explicitly included in this work. Similar to Springer *et al.*'s work,[1,7] the volume fractions of gas pores in both the GDL and the CAL were not assumed to change appreciably with the change of the operating current density, for simplicity. Due to this assumption, the transport of liquid water in the cathode was not included in this work as well.

Cathode Model

With the assumption that isothermal, isobaric, and equilibrium water vapor saturation conditions hold for a PEMFC air cathode, we developed in a previous work a steady-state polarization model.[8] In the cathode GDL, the Stefan-Maxwell multicomponent gas transport yields

$$\frac{\beta_1 + \beta_2 x}{(\beta_1 - x)(\beta_3 + \beta_2 x)}\frac{\partial x}{\partial z} = \frac{I}{4F\varphi_B^{1.5}D_{ON}^0 c_G / l_B}$$

$$\beta_1 = 1 - w, \beta_2 = D_{WN}^0/D_{OW}^0 - 1, \beta_3 = 1 - w + wD_{WN}^0/D_{OW}^0 \quad [1]$$

where x and w are the steady-state mole fractions of O_2 and water vapor in the air stream (w is fixed because isothermal and equilibrium water vapor saturation conditions are assumed), respectively, I is the steady-state operating current density, z is the spatial coordinate in the GDL normalized by its thickness l_B (see Fig. 1), F is Faraday's constant, c_G is the total gas concentration, φ_B is the volume fraction of gas pores in the GDL, and D_{ON}^0, D_{WN}^0, and D_{OW}^0 are the binary diffusion coefficients of O_2-N_2, water vapor-N_2, and water vapor-O_2, respectively. If a constant value of x at the GDL inlet is always maintained, Eq. 1 can be integrated analytically to yield

$$\frac{\beta_1(1+\beta_2)}{\beta_1\beta_2 + \beta_3}\ln\left(\frac{\beta_1 - x}{\beta_1 - x_0}\right) + \frac{\beta_3 - \beta_1}{\beta_1\beta_2 + \beta_3}\ln\left(\frac{\beta_3 + \beta_2 x}{\beta_3 + \beta_2 x_0}\right) = -\frac{I}{4F\varphi_B^{1.5}D_{ON}^0 c_G / l_B}z \quad [2]$$

which has a form similar to Eq. 5 of Springer *et al.*'s work,[7] except that I has a negative sign here for the discharging process.[8]

In the cathode CAL, the Stefan-Maxwell multicomponent gas transport yields[8]

* Electrochemical Society Student Member.
** Electrochemical Society Fellow.
z E-mail: White@engr.sc.edu

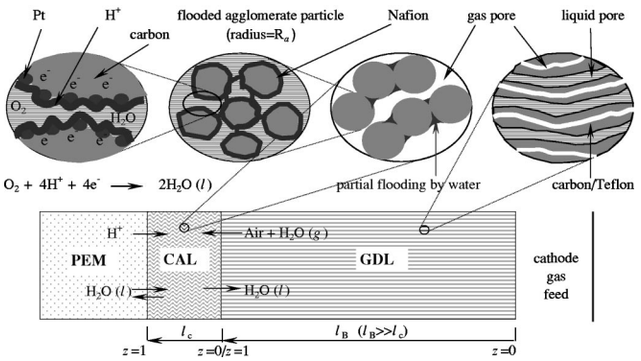

Figure 1. A schematic illustration of a PEMFC cathode.

$$\frac{\beta_1 + \beta_2 x}{(\beta_1 - x)(\beta_3 + \beta_2 x)}\frac{\partial^2 x}{\partial z^2} + \frac{\beta_4 + 2\beta_1\beta_2 x + \beta_2^2 x^2}{(\beta_1 - x)^2(\beta_3 + \beta_2 x)^2}\left(\frac{\partial x}{\partial z}\right)^2 = \frac{-j_O l_c}{\varphi_c^{1.5} D_{ON}^0 c_G / l_c}$$

$$\beta_4 = \beta_1\beta_3 - \beta_2\beta_1^2 + \beta_1\beta_2\beta_3 \quad [3]$$

where z is the spatial coordinate in the CAL normalized by its thickness l_c, φ_c is the volume fraction of gas pores in the CAL, and $-j_O$ is the steady-state consumption rate of O_2

$$-j_O = 3(1 - \varphi_c)\frac{D_{eff}}{R_a^2} c_G x H \left(\sqrt{\frac{i_{ref}}{\frac{4Fc_{ref}}{\frac{D_{eff}}{R_a^2}}}} \exp\left(-\frac{\eta}{b}\right) \right) \times \coth\left(\sqrt{\frac{i_{ref}}{\frac{4Fc_{ref}}{\frac{D_{eff}}{R_a^2}}}} \exp\left(-\frac{\eta}{b}\right) \right) - 1 \quad [4]$$

where D_{eff} is the effective diffusion coefficient of O_2 in a flooded agglomerate particle, R_a is the radius of that particle (in Ref. 10 and 11, R_a was measured to have an approximate value of 0.1 μm by using the scanning electron microscopy or the transmission electron microscopy technique), H is Henry's constant, i_{ref} is the exchange current density of the O_2 reduction reaction per unit volume of the agglomerate particles at a reference liquid phase O_2 concentration c_{ref} equal to 1.0×10^{-6} mol/cm^3 (equilibrium liquid-phase O_2 concentration when the hydrated Nafion is exposed to O_2 gas with a pressure of around 1.0 atm), b is the normal Tafel slope, and η is the overpotential. Equation 4 is obtained by solving the steady-state diffusion of O_2 inside a spherical agglomerate particle and by assuming that the overall O_2 reduction reaction follows a four-electron mechanism

$$O_2 + 4H^+ + 4e^- \rightarrow 2H_2O(l) \quad [5]$$

Equation 2 can be used to find x at the GDL/CAL interface to provide a boundary condition for Eq. 3 because

$$x|_{z=0,c} = x|_{z=1,B} \quad [6]$$

Another boundary condition for Eq. 3 is

$$\left.\frac{\partial x}{\partial z}\right|_{z=1,c} = 0 \quad [7]$$

Equation 7 is obtained by assuming zero O_2 flux at the CAL/PEM interface.

A combination of the modified Ohm's law and the conservation of charge yields[8]

$$\frac{\partial^2 \eta}{\partial z^2} = \frac{l_c}{\kappa_{eff}} 4F j_O l_c - \frac{RT}{4F}\frac{\partial^2 \ln x}{\partial z^2} \quad [8]$$

where κ_{eff} is the effective ionic conductivity of the electrolyte, R is the universal gas constant, and T is the temperature (K). To obtain Eq. 8, an infinitely large electronic conductivity is assumed for the solid phase, and a hypothetical O_2 reference electrode placed right outside the surface of a flooded agglomerate particle is used to measure the electrolyte potential.

Equation 8 is subject to the following boundary conditions

$$\left.\frac{\partial \eta}{\partial z}\right|_{z=0,c} = -\frac{RT}{4F}\left.\frac{\partial \ln x}{\partial z}\right|_{z=0,c} \quad [9]$$

and

$$\left.\frac{\partial \eta}{\partial z}\right|_{z=1,c} = \frac{l_c}{\kappa_{eff}} I \quad [10]$$

The cathode potential relative to a standard H_2 reference electrode is determined by the solid phase potential

$$\Phi_1 = (\eta + E)|_{z=1,c} \quad [11]$$

where E is the local equilibrium potential of the cathode and has a Nernst form

$$E = E_O^0 + \frac{RT}{4F}\ln(Px) \quad [12]$$

where E_O^0 is the standard potential of the cathode relative to a standard H_2 reference electrode and P is the total cathode gas pressure (atm).

It is noted that the numerical calculation of the steady-state polarization data of a PEMFC air cathode is simplified to only one region, the CAL, because the solution of x at the GDL/CAL interface is obtained analytically (see Eq. 2).

In this work, we were interested in estimating five parameters, φ_B, φ_c, i_{ref}, D_{eff}/R_a^2, and κ_{eff}, from the experimental polarization curves of a PEMFC air cathode by using the PEMFC cathode model described.

Nonlinear Parameter Estimation

Three least-squares methods are available for nonlinear parameter estimation: the steepest descent method, the Gauss-Newton method, and the Marquardt method.[12] The steepest descent method has the advantage of guaranteeing that the sum of the squared residuals S^2 will move toward its minimum without diverging but the disadvantage of slow convergence when S^2 approaches its minimum, while the Gauss-Newton method has the advantage of fast convergence when S^2 approaches its minimum but the disadvantage of diverging if the initial guesses of all the parameters are not close to their final estimates. The Marquardt method is an interpolation technique between the Gauss-Newton and the steepest descent methods. It has the advantages of the former two methods but none of their disadvantages. In general, the Marquardt method is associated with finding the parameter correction vector $\Delta\boldsymbol{\theta}$[12]

$$\Delta\boldsymbol{\theta} = (\mathbf{J}^T\mathbf{J} + \lambda\mathbf{I})^{-1}\mathbf{J}^T(\mathbf{Y}^* - \mathbf{Y}) \quad [13]$$

where $\mathbf{J}$ is a matrix of the partial derivatives of the dependent variable in a model with respect to estimation parameters evaluated at all the experimental data points, $\mathbf{Y}$ is the model prediction vector of the dependent variable, $\mathbf{Y}^*$ is the experimental observation vector of

the dependent variable, λ is the step size correction factor, **I** is the identity matrix, and the superscripts T and −1 are used to represent the transpose and inverse of a matrix, respectively. The sum of the squared residuals S^2 (unweighted) is calculated by

$$S^2 = (\mathbf{Y}^* - \mathbf{Y})^{\mathrm{T}}(\mathbf{Y}^* - \mathbf{Y}) \quad [14]$$

An algorithm of the Marquardt method consists of the following steps: (*i*) assume initial guesses for the parameter vector **θ**; (*ii*) assign a large value, *i.e.*, 1000, to λ to assure that initial parameter corrections move toward the lowered S^2; (*iii*) evaluate **J**; (*iv*) use Eq. 13 to obtain **Δθ**; (*v*) calculate the updated **θ** by

$$\boldsymbol{\theta}^{(m+1)} = \boldsymbol{\theta}^{(m)} + \Delta\boldsymbol{\theta}^{(m)} \quad [15]$$

where the superscript *m* represents the number of parameter corrections; (*vi*) calculate S^2, and reduce the value of λ if S^2 is decreased or increase the value of λ if S^2 is increased; (*vii*) repeat steps (*iii*)-(*vi*) until either S^2 does not change appreciably or **Δθ** becomes small or both are satisfied.[12]

For a model involving differential equations, the accurate calculation of **J** is important for avoiding diverging in the parameter estimation process. There are two ways to calculate **J**: the finite difference approach and the sensitivity approach.[13] A simple way to calculate $\mathbf{J}_{ij}$ at a data point *i* by the finite difference approach is the one-sided approximation

$$\mathbf{J}_{ij} = \frac{\mathbf{Y}_i(\ldots,\boldsymbol{\theta}_j + \Delta\boldsymbol{\theta}_j,\ldots) - \mathbf{Y}_i(\ldots,\boldsymbol{\theta}_j,\ldots)}{\Delta\boldsymbol{\theta}_j} \quad [16]$$

The main advantage of this approach is its convenience in coding. However, large error is sometimes generated. Two sources of error contribute to the inaccuracy in finding $\mathbf{J}_{ij}$ from Eq. 16: the rounding error arising when two closely spaced values of $\mathbf{Y}_i$ are subtracted from each other and the truncation error due to the inexact nature of Eq. 16, which is accurate only when $\Delta\boldsymbol{\theta}_j \to 0$.[13] While the truncation error decreases with a decrease in $\Delta\boldsymbol{\theta}_j$, the rounding error increases. A central finite difference approximation may be helpful to reduce the truncation error. Unfortunately, an additional numerical solution of model equations is required to find a value of $\mathbf{J}_{ij}$ compared to the one-sided approximation while the rounding error still may be significant. To eliminate the rounding error completely in the calculation of **J**, the sensitivity approach is useful. In contrast to the finite difference approach, the sensitivity approach calculates directly the derivative of a state variable with respect to a parameter, which is called the sensitivity coefficient.[13] To demonstrate, let us consider a case that the volume fraction of gas pores in the CAL, φ_c, is to be estimated alone by using the model described in the previous session. By taking the partial derivatives with respect to φ_c on both sides of Eq. 3, we obtain

$$k = \frac{i_{\mathrm{ref}}/(4Fc_{\mathrm{ref}})}{D_{\mathrm{eff}}/R_a^2}\exp\left(-\frac{\eta}{b}\right)$$

$$S_{\eta,\varphi_c} = \frac{\partial\eta}{\partial\varphi_c} \text{ and } S_{x,\varphi_c} = \frac{\partial x}{\partial\varphi_c} \quad [18]$$

By substituting $z = 1$ into Eq. 2 and taking the partial derivatives with respect to φ_c on both sides, we obtain a boundary condition for Eq. 17

$$\left[\frac{\beta_2(\beta_3 - \beta_1)}{(\beta_3 + \beta_2 x|_{z=1,\mathrm{B}})} - \frac{\beta_1(1 + \beta_2)}{(\beta_1 - x|_{z=1,\mathrm{B}})}\right]\frac{S_{x,\varphi_c}|_{z=0,c}}{\beta_1\beta_2 + \beta_3} = -\frac{I}{4F\varphi_{\mathrm{B}}^{1.5}D_{\mathrm{ON}}^0 c_{\mathrm{G}}/l_{\mathrm{B}}} \quad [19]$$

By taking the partial derivatives with respect to φ_c on both sides of Eq. 7, we obtain another boundary condition for Eq. 17

$$\left.\frac{\partial S_{x,\varphi_c}}{\partial z}\right|_{z=1,c} = 0 \quad [20]$$

Similarly, by taking the partial derivatives with respect to φ_c on both sides of Eq. 8-10, we obtain

$$\frac{\partial^2 S_{\eta,\varphi_c}}{\partial z^2} + \frac{RT}{4F}\frac{\partial^2\left(\frac{S_{x,\varphi_c}}{x}\right)}{\partial z^2} = \frac{l_c}{\kappa_{\mathrm{eff}}}4Fj_O l_c\left(\frac{S_{x,\varphi_c}}{x} - \frac{1}{1-\varphi_c} - \frac{\sqrt{k}\coth(\sqrt{k}) + k - k\coth(\sqrt{k})^2}{2b[\sqrt{k}\coth(\sqrt{k}) - 1]}S_{\eta,\varphi_c}\right) \quad [21]$$

$$\left.\frac{\partial S_{\eta,\varphi_c}}{\partial z}\right|_{z=0,c} = -\frac{RT}{4F}\left.\frac{\partial\left(\frac{S_{x,\varphi_c}}{x}\right)}{\partial z}\right|_{z=0,c} \quad [22]$$

and

$$\left.\frac{\partial S_{\eta,\varphi_c}}{\partial z}\right|_{z=1,c} = 0 \quad [23]$$

The sensitivity coefficients S_{x,φ_c} and S_{η,φ_c} can be solved numerically from Eq. 17 and 19-23, which are called the sensitivity equations,[13] if the profiles of *x* and η are known. After taking the partial derivatives with respect to φ_c on both sides of Eq. 11, we can calculate, $\mathbf{J}_i$, the partial derivative of the dependent variable Φ_1 with respect to φ_c at a steady-state current density data point i

$$\frac{\beta_1 + \beta_2 x}{(\beta_1 - x)(\beta_3 + \beta_2 x)}\frac{\partial^2 S_{x,\varphi_c}}{\partial z^2} + \frac{\beta_4 + 2\beta_1\beta_2 x + \beta_2^2 x^2}{(\beta_1 - x)^2(\beta_3 + \beta_2 x)^2}\left(\frac{\partial^2 x}{\partial z^2}S_{x,\varphi_c} + 2\left(\frac{\partial x}{\partial z}\right)\frac{\partial S_{x,\varphi_c}}{\partial z}\right) + 2\frac{\beta_5 + \beta_2^3 x^3 + 3\beta_1\beta_2^2 x^2 + (\beta_1\beta_2\beta_3 - \beta_1^2\beta_2^2 + \beta_1\beta_2^2\beta_3 + 2\beta_2\beta_4)x}{(\beta_1 - x)^3(\beta_3 + \beta_2 x)^3}\left(\frac{\partial x}{\partial z}\right)^2 S_{x,\varphi_c} = \frac{-j_O l_c}{\varphi_c^{1.5}D_{\mathrm{ON}}^0 c_{\mathrm{G}}/l_c}\left(\frac{S_{x,\varphi_c}}{x} - \frac{1.5}{\varphi_c} - \frac{1}{1-\varphi_c} - \frac{\sqrt{k}\coth(\sqrt{k}) + k - k\coth(\sqrt{k})^2}{2b[\sqrt{k}\coth(\sqrt{k}) - 1]}S_{\eta,\varphi_c}\right) \quad [17]$$

where

$$\beta_5 = \beta_1^2\beta_2\beta_3 + \beta_3\beta_4 - \beta_1\beta_2\beta_4$$

$$\mathbf{J}_i = \left(\frac{\partial \Phi_1}{\partial \varphi_c}\right)_i = \left[S_{\eta,\varphi_c}\big|_{z=1,c} + \frac{RT}{4F}\left(\frac{S_{x,\varphi_c}}{x}\right)\Big|_{z=1,c}\right]_i \quad [24]$$

If several parameters are to be estimated at the same time, in a similar manner, we can obtain some corresponding sensitivity equations and calculate $\mathbf{J}_{ij}$, the partial derivative of the dependent variable Φ_1 with respect to parameter θ_j at a current density data point i

$$\mathbf{J}_{ij} = \left(\frac{\partial \Phi_1}{\partial \theta_j}\right)_i = \left[S_{\eta,\theta_j}\big|_{z=1,c} + \frac{RT}{4F}\left(\frac{S_{x,\theta_j}}{x}\right)\Big|_{z=1,c}\right]_i \quad [25]$$

The main advantage of the sensitivity approach is its accuracy in finding **J** without demanding more computer time, even if it is less friendly for coding compared to the finite difference approach.

In this work, the Marquardt method was combined with the sensitivity approach for the estimation of parameters of interest from the experimental steady-state polarization data of a PEMFC air cathode. After scrutinizing the model equations described in the previous session, we find that φ_B, φ_c, i_{ref}, D_{eff}/R_a^2, and κ_{eff} are important parameters and their values should be obtained before the accurate prediction of the performance of a cathode is possible. Among them, φ_B, φ_c, i_{ref}, and κ_{eff} are the physical meaningful parameters, and the reciprocal of D_{eff}/R_a^2 can be interpreted as the time constant for O_2 diffusion inside a flooded agglomerate particle.

The normal Tafel slope b is a kinetics parameter, which value was measured and reported in the literature.[14-18] This parameter was not included in our estimation. The thicknesses of the GDL and the CAL were measured on a gas diffusion electrode. They were not included in our estimation as well.

From a statistical point of view, it is more desirable to obtain a confidence interval of a parameter rather than to simply obtain its point estimate. In this work, the 95% confidence interval of a parameter θ_j is constructed by[12]

$$\boldsymbol{\theta}_j^* - t_{(t-0.05/2)} S_E \sqrt{\mathbf{a}_{jj}} \leqslant \boldsymbol{\theta}_j < \boldsymbol{\theta}_j^* + t_{(1-0.05/2)} S_E \sqrt{\mathbf{a}_{jj}} \quad [26]$$

where $\boldsymbol{\theta}_j^*$ represents the point estimate of parameter $\boldsymbol{\theta}_j$, $t_{(1-0.05/2)}$ is a value of Student's t distribution with $(n - m)$ degrees of freedom where n and m are the numbers of experimental data points and estimation parameters, respectively, $\mathbf{a}_{jj}$ is a diagonal element of the matrix $(\mathbf{J}^T\mathbf{J})^{-1}$, and S_E is the standard deviation and can be calculated by

$$S_E^2 = \frac{\Sigma_{i=1}^{n}[(\Phi_1)_i - (\Phi_1^*)_i]^2}{n - m} \quad [27]$$

where Φ_1^* is the experimental cathode potential. For a nonlinear model, due to correlations between parameter pairs, the calculated confidence intervals are not as rigorous as those for a linear model, and a joint confidence region of all the estimation parameters is expected to be more useful for identifying their true region. The 95% joint confidence region of estimation parameters can be obtained by[12]

$$\frac{(\boldsymbol{\theta}^* - \boldsymbol{\theta})^T(\mathbf{J}^T\mathbf{J})(\boldsymbol{\theta}^* - \boldsymbol{\theta})}{mS_S^2} \leqslant F_{(1-0.05)}(m, n - m) \quad [28]$$

where $F_{(1-0.05)}(m,n - m)$ is a value of the F distribution with m and $(n - m)$ degrees of freedom.

Numerical Method

A three-point finite difference method was used to approximate each derivative variable in a differential equation, and a general nonlinear equation solver in FORTRAN called GNES was used to carry out all the numerical calculations. An important feature of this solver is its convenience in coding and debugging. Normally, only model equations are required. The Jacobian matrix for their numerical calculation is not required, because the solver can generate it internally by using a forward finite difference approximation method without sacrificing much numerical efficiency. For further improvement of numerical efficiency, however, a user may elect to provide a banded Jacobian matrix to the solver.

To find the parameter correction vector $\Delta\boldsymbol{\theta}$ by using Eq. 13, one needs to calculate the model prediction vector **Y** and the matrix **J**. Therefore, the numerical solutions of Φ_1, $\partial\Phi_1/\partial\varphi_B$, $\partial\Phi_1/\partial\varphi_c$, $\partial\Phi_1/\partial i_{ref}$, $\partial\Phi_1/\partial(D_{eff}/R_a^2)$, and $\partial\Phi_1/\partial\kappa_{eff}$ at each current density data point were required. One may consider coupling five sets of sensitivity equations such as Eq. 17 and 19-23 to the original model equations and solving them at the same time. However, we elected to choose a decoupling method in our numerical calculations. The decoupling of model equations from sensitivity equations saves computer time due to the following concerns: (*i*) The computer time required for performing the LU decomposition on six matrices of the same size, *i.e.*, $n \times n$, is less than that required for performing the decomposition on a single matrix of a sixfold size, *i.e.*, $6n \times 6n$ (the LU decomposition method is used by GNES in its numerical calculation). (*ii*) The coupling of five sets of sensitivity equations, which are linear with respect to all the sensitivity coefficients and do not require iterations for their numerical solutions, to the model equations, which are nonlinear with respect to their state variables such as x and η and require iterations for their numerical solutions, inevitably force all the sensitivity equations to undergo the same number of iterations before all the converged solutions are obtained. An efficient numerical algorithm is important for a nonlinear parameter estimation problem with a sophisticated differential equation model such as the model considered in this work, because many numerical calculations are usually necessary before the final parameter estimates are obtained. After providing a banded Jacobian matrix to the solver and calculating the model equations (to be solved first) and each set of sensitivity equations separately, only 1 min was required by a personal computer with an 866 MHz CPU to obtain one parameter correction vector (84 experimental data point were considered, and 100 node points were used to discretize the spatial coordinate z).

Experimental

The procedures for making a membrane electrode assembly (MEA) in this work were similar to those described in the literature.[19] The Pt catalyst ink with 75 wt % catalyst and 25 wt % Nafion ionomer (dry content) was prepared with an experimentally available 40.2 wt % Pt/Vulcan XC-72 catalyst (E-TEK Division, De Nora North America, NJ) and a perfluorosulfonic acid-copolymer (Alfa Asesar, MA). The ink was mixed properly for at least 8 h. ELAT GDLs (E-TEK Division, De Nora North America, NJ), which thickness was measured to be approximately 400 μm, were cut into 3.2×3.2 cm^2 pieces. The catalyst ink was sprayed onto the GDLs and dried for 1/2 hour to evaporate any remaining solvent. This process was repeated until the target loading was achieved. The catalyzed GDLs, which served as both the anode and the cathode, were calculated to have a Pt loading of 0.5 mg/cm^2 and measured to have a CAL thickness of 15 μm. To make an MEA, two pieces of catalyzed GDLs were bonded to a pretreated Nafion 112 membrane by hot pressing at 140°C for 2 min under a pressure of 500 psig. The MEA was assembled into a test fuel cell with single-channel serpentine flow field graphite end plates purchased from Fuel Cell Technologies.

The test fuel cell was operated on a 120 A fuel cell test station (Fuel Cell Technologies). The temperatures of the test cell and the cathode gas humidifier were set to be 70°C, while the temperature of the anode gas humidifier was set at 10°C more in order to avoid the partial dehydration of the PEM on the anode side at high operating current densities. The test fuel cell was first operated at 0.6 V under the ambient gas pressure for at least 8 h with a 250 cm^3/min O_2 flow rate on the cathode side and a 180 cm^3/min H_2 flow rate on the anode side. Then the cathode gas feeding was switched to air with a

Table I. Parameters used for the steady-state polarization model of a PEMFC cathode operated at 70°C.

Parameter	Value	Comments
D^0_{ON}	0.230 cm^2/s	Ref. 20 (T = 316 K, P = 1 atm)[a]
D^0_{OW}	0.282 cm^2/s	Ref. 20 (T = 308 K, P = 1 atm)[a]
D^0_{NW}	0.293 cm^2/s	Ref. 20 (T = 298 K, P = 1 atm)[a]
l_B	0.04 cm	Measured on E-TEK GDL
l_c	0.0015 cm	Measured
b	0.0261 V[b]	Ref. 14-18
H	0.0277 $[mol/cm^3(l)]/[mol/cm^3(g)]$	Ref. 17
E^0_O	1.20 V	Ref. 17

[a] $D^0_{ij}(T,P) = D^0_{ij}(T_1,P_1) \times \frac{P_1}{P} \times \left(\frac{T}{T_1}\right)^{1.8}$

[b] A value on a Φ_1 *vs.* $\ln(-I)$ plot.

flow rate of 720 cm^3/min. The flow rate of H_2 was increased to be 640 cm^3/min. High flow rates on both the cathode and the anode were employed in this work in order to maintain a constant mole fraction of O_2 at the cathode GDL inlet and to support the largest current attainable on a H_2/air PEMFC during the steady-state polarization curve measurements. The anode gas pressure was set to be 1.3 atm, a value that makes the partial pressure of H_2 in the anode gas pores equal to 1.0 atm, while three different values, 1.3, 2.3, and 3.3 atms, were used for the cathode gas pressures. After a new cathode gas pressure was set, the cell was first operated at 0.6 V for at least 30 min, and then a steady-state polarization curve was measured. To measure a polarization curve of a PEMFC, the cell potential was swept from 1.0 to 0.1 and to 1.0 V with a step size of 25 mV and a delay time of 15 s. To obtain a polarization curve of the air cathode, the voltage drop across the PEM was used to correct the polarization curve of a full cell. Because the PEM resistance is unlikely to be a strong function of the operating current density if a thin PEM is used and good anode gas humidification is always guaranteed, we assumed the existence of a constant value of the PEM resistance in this work during each polarization curve measurement and used Ohm's law to calculate the voltage drop across the PEM at each current density data point. The PEM resistance was measured at 10 KHz with a Hewlett Packard/Agilent 4263B LCR meter at the open-circuit conditions immediately after each polarization curve was measured. In this work, the same value of 78 mΩ cm^2 was obtained for the PEM resistance in all the measurements.

Results and Discussion

In our model, the values of some parameters such as D^0_{ON}, D^0_{OW}, D^0_{NW}, l_B, l_c, b, H, and E^0_O can be obtained accurately from either direct measurements or the literature.[14-18,20] They are presented in Table I. The remaining five parameters, φ_B, φ_c, i_{ref}, D_{eff}/R_a^2, and κ_{eff} have to be estimated from the experimental polarization curves. Springer *et al.*[1] suggested that the simultaneous fit of several sets of experimental data measured under different operating conditions provides one with more effective diagnostics than a fit of only one set of experimental data at a time. In this work, our model was used to fit three experimental polarization curves of an air cathode simultaneously. To demonstrate the goodness of the simultaneous fit, our model was also used to fit each experimental curve independently, for comparison purposes. The 95% confidence intervals of all five parameters obtained from the simultaneous fit are presented in Table II. The polarization curve predictions after the simultaneous fit are compared to three experimental curves in Fig. 2a and b. In general, a satisfactory match of model predictions with experimental curves can be observed from these two figures. Therefore, the simultaneous fit was performed effectively.

One may want to know whether or not there is further improvement of a fit if only one experimental curve is considered at a time for the parameter estimation. The 95% confidence intervals of all the five parameters obtained from three independent fits are also presented in Table II. The polarization curve predictions after these independent fits are compared to experimental curves in Fig. 3. Even if Table II shows that each independent fit leads to a smaller S_E compared to the simultaneous fit, it is hard for one to simply conclude that Fig. 3 displays much better fits than Fig. 2a.

One may notice from the results of three independent fits presented in Table II that with the decrease of the cathode gas pressure, the value of κ_{eff} decreases, while the values of i_{ref} and D_{eff}/R_a^2 increase. An exclusive explanation for all these phenomena is difficult to find. One may attribute the decrease of κ_{eff} to the expansion effect of the CAL thickness with a decrease in cathode gas pressure. Unfortunately, the increases of D_{eff}/R_a^2 and i_{ref} cannot be answered properly by this explanation. Alternately, one may attribute the decrease of κ_{eff} and the increase of D_{eff}/R_a^2 with a decrease in gas pressure to the partial Nafion ionomer dehydration in the CAL. (The highest current density obtainable on a low-pressure air cathode is smaller than that obtainable on a high-pressure air cathode. Assume that the amount of liquid water maintained in the CAL decreases with a decrease in current density. Due to less water content in the CAL of a low-pressure air cathode, small gas pores may be left open in an agglomerate particle to facilitate O_2 diffusion to the catalyst sites.) However, the increase of i_{ref} with a decrease in gas pressure remains unexplained. As noticed from Fig. 2a and 3, our model predictions do not match experimental curves in the medium-current-density range. A proper understanding of this phenomenon is probably useful for explaining the changes of κ_{eff}, i_{ref}, and D_{eff}/R_a^2 with gas pressure. We recall that the values of φ_B and φ_c are assumed to be independent of the operating current density in this work. Rigorously speaking, it is not true. A small operating current density is expected to incur a small liquid water flux out of the cathode GDL and consequently cause a small number of gas pores in the GDL to be flooded. A large operating current density is expected to incur a large liquid water flux out of the GDL and consequently cause many gas pores in the GDL to be flooded. Therefore, the values of φ_B and

Table II. Comparison of the 95% confidence intervals estimated from the simultaneous fit of three experimental polarization curves and the 95% confidence intervals estimated from the independent fits.

	Simultaneous fit	Independent fit (P = 1.3 atm)	Independent fit (P = 2.3 atm)	Independent fit (P = 3.3 atm)
φ_B	$0.1991 \pm 6.676 \times 10^{-4}$	$0.2013 \pm 2.521 \times 10^{-3}$	$0.1980 \pm 1.019 \times 10^{-3}$	$0.1966 \pm 6.341 \times 10^{-4}$
φ_c	$(3.933 \pm 0.2578) \times 10^{-2}$	$(3.366 \pm 0.3669) \times 10^{-2}$	$(3.925 \pm 0.6124) \times 10^{-2}$	$(4.216 \pm 0.7155) \times 10^{-2}$
i_{ref} (A/cm^3)	$(7.198 \pm 0.8226) \times 10^{-4}$	$(1.036 \pm 0.1829) \times 10^{-3}$	$(6.408 \pm 1.409) \times 10^{-4}$	$(5.152 \pm 1.081) \times 10^{-4}$
D_{eff}/R_a^2 (s^{-1})	[a]$(3.052 \pm 1.637) \times 10^3$	$(8.173 \pm 16.46) \times 10^3$	$(2.226 \pm 2.605) \times 10^3$	$(1.534 \pm 1.694) \times 10^3$
κ_{eff} (S/cm)	$(9.947 \pm 1.004) \times 10^{-3}$	$(7.750 \pm 2.230) \times 10^{-3}$	$(1.207 \pm 0.2822) \times 10^{-2}$	$(1.468 \pm 0.3385) \times 10^{-2}$
S_E (V)	1.239×10^{-2}	0.8916×10^{-2}	1.010×10^{-2}	0.9766×10^{-2}

[a] If the value of D_{eff} is assumed to be 2.199×10^{-6} cm^2/s,[8] the value of R_a is found to be in the range of $0.2165 \leq R_a < 0.3942$ μm, which is generally consistent with the values reported in Ref. 10 and 11.

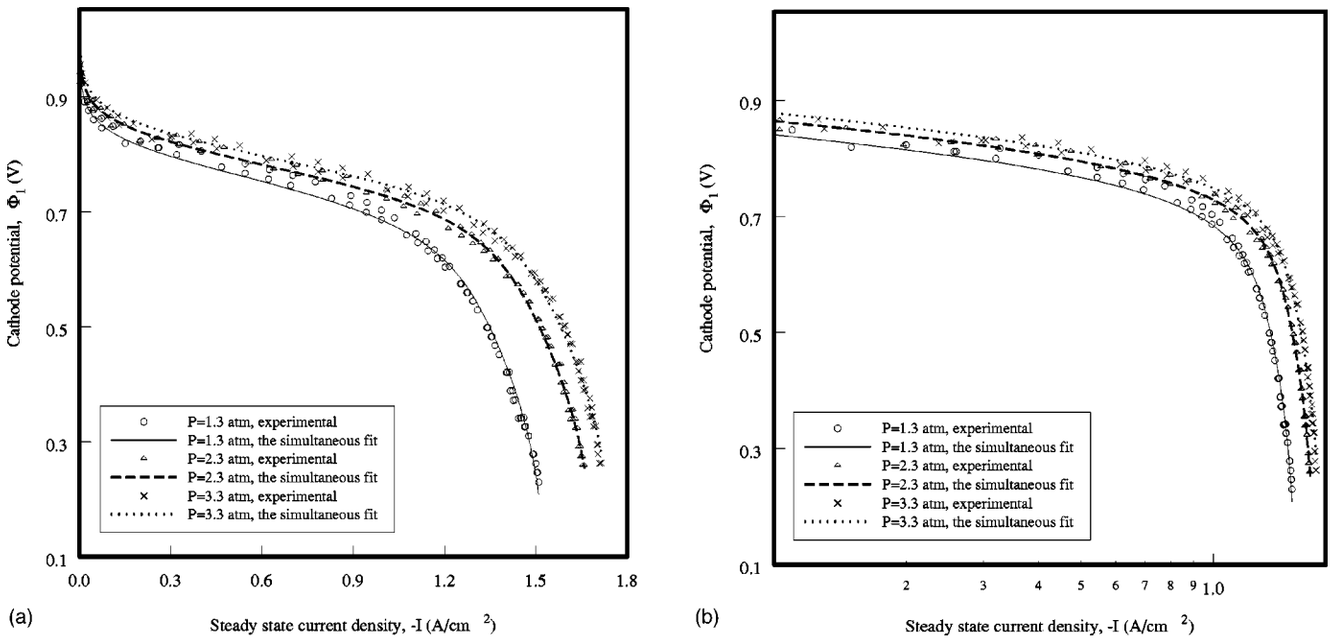

Figure 2. (a, left) Comparison of the polarization curve predictions of a PEMFC air cathode and three experimental curves. The point estimates obtained from the simultaneous fit were used for their corresponding parameters in the predictions. (b, right) A replot of (a) in a log scale.

φ_c in the medium-current-density range are expected to be larger than those in the high-current-density range. Even if the extracted values of φ_B and φ_c presented in Table II are not noticed to vary appreciably with a change in gas pressure, the possibility that these values change with the operating current density is not excluded. A proper modeling of the transport of liquid water in both the GDL and the CAL in a manner similar to that introduced in Ref. 5, where Darcy's law was used, is expected to take into account the changes of φ_B and φ_c with current density and improve our polarization curve predictions. In this work, all the experimental polarization curves of a PEMFC were measured by sweeping the cell potential in both the forward and backward directions, and an effort to discriminate part of our experimental data obtained from one particular direction was not attempted. Because of this, there was appreciable difference between the experimental data measured in two potential sweep directions in the medium-current-density range. This difference could be explained by the hysteresis behavior of a PEMFC cathode associated with liquid water inhibition and drainage in the GDL.[21-23] This hysteresis behavior, which was particularly significant for a low-pressure cathode (see Fig. 2a and 3), introduced appreciable noise to our experimental data. In this work, a delay time of 15 s was used to measure all the experimental polarization curves. This delay time is shorter than that used in Ref. 10. The use of longer delay time will probably be helpful for reducing the hysteresis behavior of a cathode.

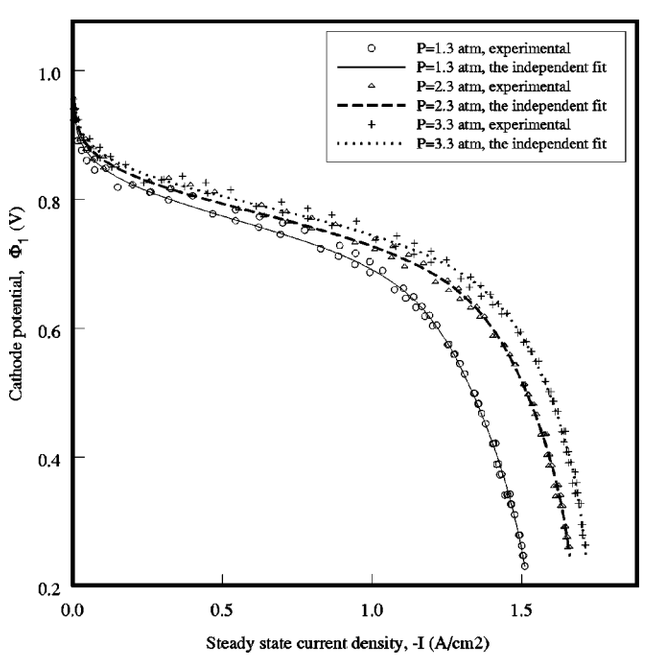

Figure 3. Comparison of the polarization curve predictions of a PEMFC air cathode and three experimental curves. The points estimates obtained from each independent fit were used for their corresponding parameters in the predictions.

One may also notice from Table II that the confidence interval of D_{eff}/R_a^2 is much larger than that of any of the other four parameters. This indicates some uncertainty in the determination of D_{eff}/R_a^2. A large confidence interval of a parameter was also obtained by Evans and White.[24] They explained that an unacceptably large confidence interval of a parameter was related to parameter correlations in a nonlinear model. To verify this explanation, we fixed all the other four parameters and estimated the parameter D_{eff}/R_a^2 alone from a simultaneous fit of three experimental curves. Because only one parameter was left for estimation, parameter correlations were removed. As expected, in the absence of parameter correlations, a much smaller confidence interval of D_{eff}/R_a^2 was obtained: $2.792 \times 10^3 \leqslant D_{\text{eff}}/R_a^2 < 3.312 \times 10^3\ \text{s}^{-1}$.

The degree of correlation between any two parameters in our nonlinear model can be appreciated by looking at the correlation coefficient matrix **R** obtained from $(\mathbf{J}^T\mathbf{J})^{-1}$ (see Ref. 12) after the simultaneous fit

$$\mathbf{R} = \begin{bmatrix} 1.000 & 0.5176 & 0.3113 & -0.05743 & -0.9070 \\ 0.5176 & 1.000 & 0.3357 & -0.6786 & -0.4223 \\ 0.3113 & 0.3357 & 1.000 & -0.5072 & -0.1819 \\ -0.05743 & -0.6786 & -0.5072 & 1.000 & -0.2339 \\ -0.9070 & -0.4223 & -0.1819 & -0.2339 & 1.000 \end{bmatrix} \quad [29]$$

where for either the subscript i or the subscript j of the element $\mathbf{R}_{ij}$, 1 represents φ_B, 2 represents φ_c, 3 represents i_{ref}, 4 represents D_{eff}/R_a^2, and 5 represents κ_{eff}.

As explained in Ref. 12, the higher the correlation between two parameters, the closer the absolute value of $\mathbf{R}_{ij}$ is to 1.0. One can observe from Eq. 29 that the values of all the diagonal elements of **R** are equal to 1.0. This indicates that each parameter is highly correlated with itself. One can also observe from Eq. 29 that the highest correlation between two different parameters occurs to the $\varphi_B - \kappa_{eff}$ pair, and the lowest correlation between two different parameters occurs to the $\varphi_B - D_{eff}/R_a^2$ pair. The correlations between the $\varphi_c - D_{eff}/R_a^2$ pair, the $i_{ref} - D_{eff}R_a^2$ pair, and the $\varphi_B - \varphi_c$ pair are also high. Reference 12 explains that a positive correlation coefficient between two parameters implies that the errors causing the estimate of one parameter to be high also cause the other to be high, and a negative correlation coefficient implies that the errors causing the estimate of one parameter to be high cause the other to be low. Because the $\varphi_B - \kappa_{eff}$ pair has a negative correlation coefficient, it is not hard for one to conclude that if κ_{eff} is underestimated, an overestimation of φ_B results.

We know from Ref. 12 that for a linear model, all the estimation parameters are uncorrelated, the axes of the confidence ellipsoid is parallel to the coordinates of the parameter space, and the individual parameter confidence intervals hold for each parameter independently; whereas for a nonlinear model, the parameters are correlated, the axes of the confidence ellipsoids are at an angle to the parameter space, and the individual parameter confidence limits do not represent the true interval within which a parameter may lie. Therefore, the confidence intervals presented in Table II are not rigorously valid, and a joint confidence region of all the parameters is expected to be more useful. In this work, the 95% joint confidence region of all the five parameters can be obtained from the simultaneous fit by Eq. 30 and 31

$$(\Delta\theta)^T \begin{bmatrix} 3.768 \times 10^4 & 7.056 \times 10^3 & 7.095 \times 10^4 & 1.559 \times 10^{-2} & 3.739 \times 10^4 \\ 7.056 \times 10^3 & 2.033 \times 10^3 & 1.995 \times 10^4 & 4.036 \times 10^{-3} & 8.298 \times 10^3 \\ 7.095 \times 10^4 & 1.995 \times 10^4 & 3.307 \times 10^5 & 4.373 \times 10^{-2} & 8.604 \times 10^4 \\ 1.559 \times 10^{-2} & 4.036 \times 10^{-3} & 4.373 \times 10^{-2} & 8.548 \times 10^{-9} & 1.769 \times 10^{-2} \\ 3.739 \times 10^4 & 8.298 \times 10^3 & 8.604 \times 10^4 & 1.769 \times 10^{-2} & 4.017 \times 10^3 \end{bmatrix} (\Delta\theta) \leqslant 1.729 \times 10^{-3} \quad [30]$$

where

$$\Delta\theta = \begin{bmatrix} \varphi_B - 0.1991 \\ \varphi_c - 3.933 \times 10^{-2} \\ i_{ref} - 7.198 \times 10^{-4} \\ D_{eff}/R_a^2 - 3.052 \times 10^3 \\ \kappa_{eff} - 9.947 \times 10^{-3} \end{bmatrix} \quad [31]$$

The disadvantage of using Eq. 30 and 31 is the lack of straightforwardness in identifying the region where all the parameters lie. One may fix the values of some parameters and determine the confidence region of the remaining parameters. For instance, if the values of φ_B, φ_c, i_{ref}, and κ_{eff} in Eq. 30 and 31 are fixed to their respective point estimates obtained from the simultaneous fit, one can obtain the 95% confidence region of D_{eff}/R_a^2

$$2.603 \times 10^3 \geqslant D_{eff}/R_a^2 < 3.502 \times 10^3 \ \text{s}^{-1} \quad [32]$$

To appreciate the goodness of the polarization curve predictions by using a parameter value defined by a joint confidence region rather than by a confidence interval, a comparison of several simulated polarization curves of a medium-pressure air cathode ($P = 2.3$ atm) is shown in Fig. 4a and b. While the values of all the other four parameters in the polarization curve simulations were fixed to their respective point estimates obtained from the simultaneous fit, the values of D_{eff}/R_a^2 were assigned by both the upper and the lower limits defined by its 95% confidence interval and those defined by the 95% confidence region (Eq. 32). One can notice from these two figures that the parameter D_{eff}/R_a^2 values defined by the confidence region leads to less uncertainty in model predictions than those defined by the confidence interval.

If PEMFCs are widely used to power the electric vehicles in the future, their cathodes are likely going to be operated with low-pressure air due to the energy cost of gas pressurizing. Therefore, a proper evaluation of mass-transport limitations in a low-pressure PEMFC cathode is important. The distribution of the mole fraction of O_2 across the CAL of a low-pressure air cathode ($P = 1.3$ atm) operated at different current densities are presented in Fig. 5. The point estimates obtained from the simultaneous fit were used by their corresponding parameters for the calculation of all the x distributions. In general, the value of x decreases in the direction toward the PEM. With the increase of the operating current density, the value of x at the GDL/CAL interface decreases as well due to gas-phase transport loss of O_2 in the GDL.[8] When the current density increases to a value as high as 1.5 A/cm^2, except for a small region close to the GDL/CAL interface, all the other CAL region has a negligible O_2 content. As noticed in Fig. 2a, the value of 1.5 A/cm^2 is close to the limiting current of the low-pressure air cathode ($P = 1.3$ atm). Therefore, the gas-phase transport limitation across the GDL is responsible for a limiting current measured on an air cathode. A similar conclusion was also drawn in the literature.[1,4]

Another way to evaluate mass-transport limitations in a low-pressure air cathode ($P = 1.3$ atm) is to look at the dimensionless O_2 reduction current density distribution, $4Fj_Ol_c/I$, in the CAL. If there is a uniform distribution of O_2 reduction current density in the CAL, $4Fj_Ol_c/I$ is equal to unity for all the spatial node points. The dimensionless $4Fj_Ol_c/I$ *vs.* z plots are presented in Fig. 6 for different operating current densities. When the current density is low, *i.e.*, $-I = 0.05$ A/cm^2, an almost uniform distribution of O_2 reduction current density exists. At such current density, the cathode performance is mainly dominated by slow Tafel kinetics.[3] When the current density becomes higher, *i.e.*, $-I = 0.5$ A/cm^2, a nonuniform distribution of O_2 reduction current density in the CAL is observed, and the reaction at the CAL/PEM interface is favored. At such current density, the cathode performance is likely influenced by both processes: slow ionic conduction and slow Tafel kinetics (justification discussed later).[3] When the current density becomes even

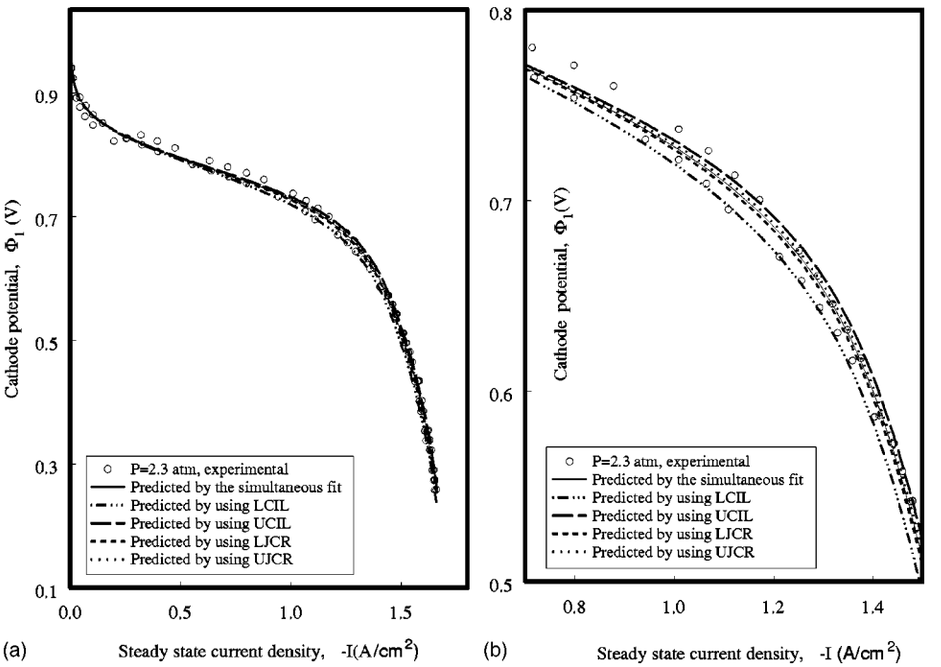

Figure 4. (a) Comparison of the polarization curve predictions of a medium-pressure PEMFC air cathode ($P = 2.3$ atm) using different limits of the parameter D_{eff}/R_a^2 obtained from the 95% confidence interval and 95% joint confidence region. Point estimates obtained from the simultaneous fit were used for the other four parameters. LJCR and UJCR represent the lower and upper joint confidence region limits, respectively; LCIL and UCIL represent the lower and upper confidence interval limits, respectively. (b) A replot of (a) in the potential range 0.5-0.8 V.

higher, *i.e.*, $-I = 1.2$ A/cm^2, high O_2 reduction current density is seen not only in a region close to the CAL/PEM interface but also in a region close to the GDL/CAL interface. At such current density, the cathode performance is likely influenced jointly by slow gas-phase mass transport and slow ionic conduction (justification discussed later).[3] When the current density is as high as 1.5 A/cm^2, O_2 reduction reaction occurs predominantly at the GDL/CAL interface. At such current density, O_2 gas is depleted in most of the CAL except for a small region close to the GDL/CAL interface (Fig. 5), and the cathode performance is limited by the gas-phase transport across the GDL.[1]

To gain further understanding as to how the performance of a

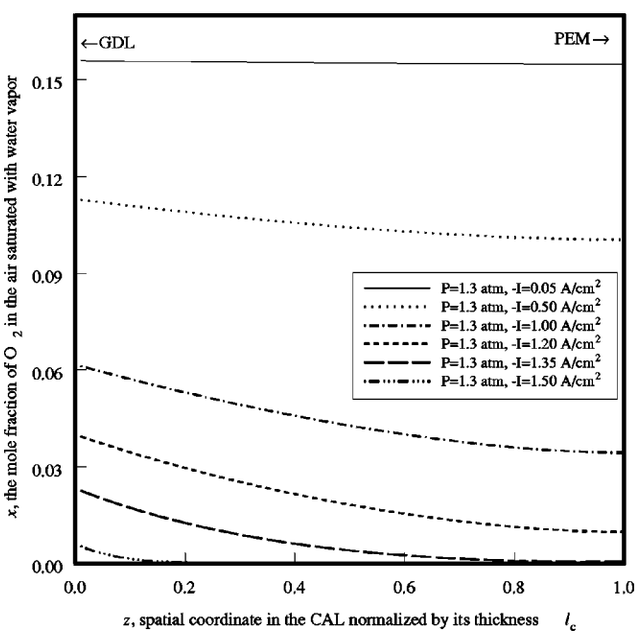

Figure 5. Distribution of the mole fraction of O_2 in the catalyst layer of a low-pressure PEMFC air cathode ($P = 1.3$ atm) with the change of the operating current density, $-I$.

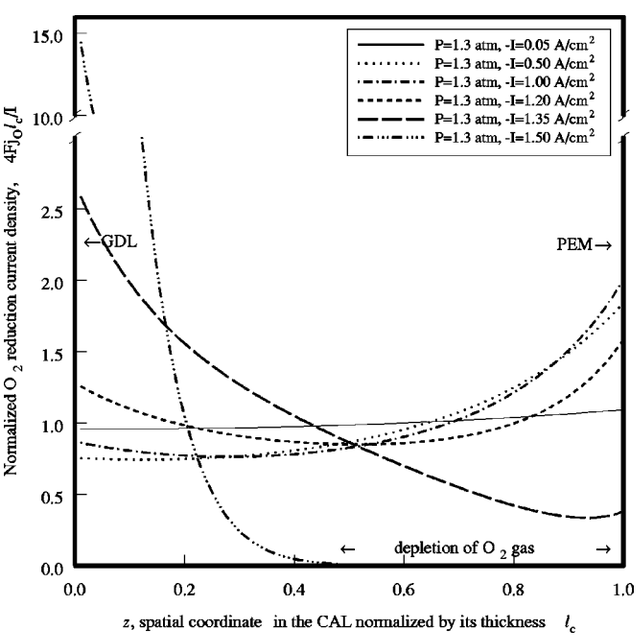

Figure 6. Distribution of the dimensionless O_2 reduction current density in the catalyst layer of a low-pressure PEMFC air cathode ($P = 1.3$ atm) with the change of operating current density.

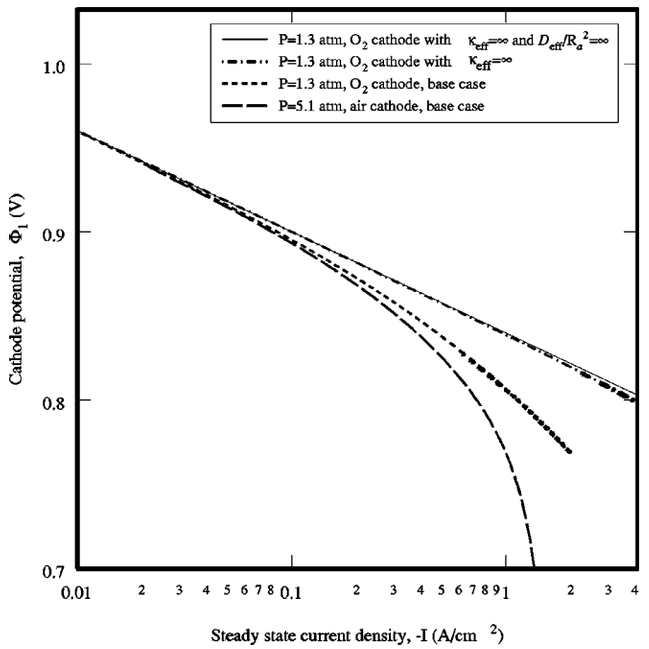

Figure 7. Comparison of the simulated polarization curves of a high-pressure air cathode ($P = 5.1$ atm) and three low-pressure O_2 cathodes ($P = 1.3$ atm). Unless indicated otherwise on a plot, the point estimates obtained from the simultaneous fit were assigned to all the parameters in the simulations.

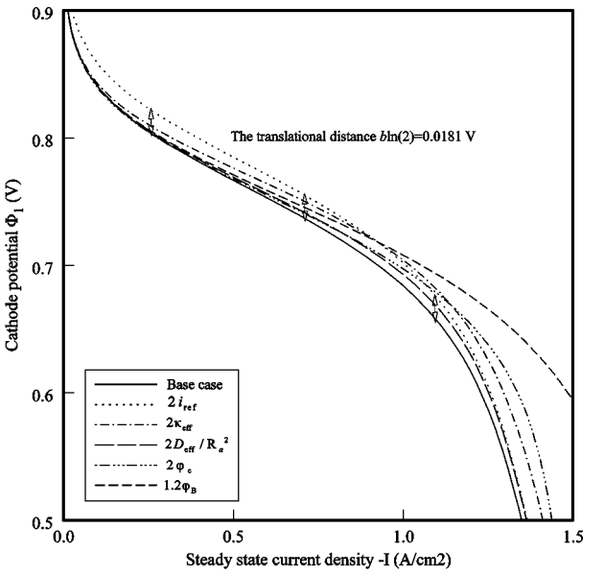

Figure 8. Comparison of the simulated polarization curves of a low-pressure PEMFC air cathode ($P = 1.3$ atm). Except for the parameter values indicated on a plot, the point estimates obtained from the simultaneous fit were assigned to all the remaining parameters in the simulations.

cathode is dominated by one or more slow processes with the change of current density, it is helpful to look at Fig. 7, where the simulated steady-state polarization curve of a cathode fed with high-pressure air ($P = 5.1$ atm) is compared to the simulated curves of three cathodes fed with low-pressure O_2 ($P = 1.3$ atm). Two different values of gas pressure are chosen for the four cathodes in the simulations such that the partial pressure of O_2 at the GDL inlet is the same (1 atm) for each cathode, and all the predicted polarization curves are expected to agree in the low-current-density region where the sluggish Tafel kinetics is the only dominating process. Among three O_2 cathodes, an infinitely large value of κ_{eff} was assumed for one O_2 cathode, and the infinitely large values of both κ_{eff} and $D_{\text{eff}}/R_{\text{a}}^2$ were assumed for another O_2 cathode. For the latter cathode, due to the disappearance of ionic conduction limitation and liquid-phase O_2 diffusion limitation, the cathode behaves like a planar electrode and a normal Tafel slope is always presented. For the former cathode, the cathode behaves like a thin-film diffusion electrode and the possible change of Tafel slope due to slow liquid-phase O_2 diffusion is reflected. One may notice by comparing the polarization curves of three O_2 cathodes in Fig. 7 that for the base case O_2 cathode (point estimates obtained from the simultaneous fit in this work were assigned to all the parameters), the change of Tafel slope is mainly due to the importance of slow ionic conduction, and the influence of O_2 diffusion in an agglomerate particle seems to be insignificant until the current density is high, *i.e.*, $-I = 4$ A/cm^2. For the base case air cathode, the change of Tafel slope due to gas-phase transport loss of O_2 starts to be observable even when the operating current density is not high. It is also possible that the agglomerate particle diffusion of O_2 influences the air cathode performance when the current density approaches the limiting current, because the O_2 reduction reaction is limited to a small region close to the GDL/CAL interface at such current density (see the curve with $-I = 1.5$ A/cm^2 in Fig. 6).

The optimization of a PEMFC is usually associated with overcoming one or more mass-transport limitations. In this work, the influence of the change of the value of a parameter on the cathode performance was briefly studied and presented in Fig. 8, where the point estimates of all five parameters obtained from the simultaneous fit were used for the base case simulation, and only one parameter value was allowed to change from the base case for the simulation of any other curve. One can observe from Fig. 8 that any increase of φ_{B}, φ_{c}, i_{ref}, κ_{eff}, and $D_{\text{eff}}/R_{\text{a}}^2$ leads to an improvement of the cathode performance. Among them, the increase of φ_{B} influences the limiting current value most effectively. One may want to know whether or not a significant improvement of the performance of an air cathode is possible by using a GDL with a larger volume fraction of gas pores and a smaller thickness, because both of them lead to the decrease of gas-phase transport loss of O_2. In one of our experiments (not published), we tested a specially designed PEMFC by using a porous, approximately 200 μm thick GDL (many large open pores were observed on the GDL against the light) to make the cathode, and noticed that the performance of this cell was even worse than that observed on a cell with the use of a regular GDL to make the cathode. However, one should not conclude from this experiment that the decrease of the GDL thickness or the increase of the volume fraction of gas pores in the GDL does not lead to an improvement of the cathode performance. The presence of many large open pores in the GDL could be very harmful to the cathode, because large pores were likely to lead to a quick loss of liquid water in the CAL and consequently lead to the decrease of the electrolyte conductivity. We would like to believe that it is important to maintain a sufficient amount of liquid water in the CAL to make Nafion ionomer fully hydrated. If one is able to make a thinner GDL without introducing many big open pores, better performance should be expected on a cathode with such GDL. One can also observe from Fig. 8 that except for the current density range close to the limiting current density value, the increase of i_{ref} improves the cathode performance more significantly than the increase of any other parameter. This is because an increase of i_{ref} is predicted by our model to cause the vertical translational movement of an entire polarization curve to a place at higher potentials.[8] The translational distance $\Delta\Phi_1$ due to an increase in i_{ref}, Δi_{ref} can be determined by[8]

$$\Delta\Phi_1 = b \ln\left(1 + \frac{\Delta i_{\text{ref}}}{i_{\text{ref}}}\right) \quad [33]$$

Table III. Comparison of the computer time required by a personal computer with an 866 MHz CPU for the calculation of nonlinear model equations.

	With banded Jacobian matrix (user-supplied)	With banded Jacobian matrix (not user-supplied)	With dense Jacobian matrix (not user-supplied)
Calculating 200 nonlinear model equations six times	1.27 s	2.07 s	31.3 s
Calculating 1200 nonlinear model equations once	1.64 s	7.35 s	188 s
Numerical efficiency summary	Good	Fair	Poor

Even if it seems that one can increase the value of i_{ref} by increasing the weight percentage of the catalyst Pt in the Pt/C composites, it is tricky to realize this in practice, because with the increase of this weight percentage, the particle size of Pt tends to grow and the specific surface area of Pt tends to decrease.[25] If the value of i_{ref} is proportional to the surface area of Pt per unit volume of the CAL, an increase in the weight percentage of Pt will not always guarantee the increase of i_{ref}. One can also observe from Fig. 8 that the cathode performance is improved effectively over a wide range of the operating current density due to an increase in κ_{eff}, whereas the improvement of the cathode performance due to an increase in either D_{eff}/R_a^2 or φ_c is effective only in the high-current-density range. In our previous study on the κ_{eff} profile of an air cathode,[26] we concluded that there was an optimal amount of Nafion ionomer loading in the CAL of a cathode (ELAT electrode). Either too much or too small Nafion loading did not lead to good performance of a cathode. Besides, a nonlinear ionic conductivity distribution in the cathode CAL was noticed. The existence of a nonlinear ionic conductivity distribution on an ELAT electrode is understandable because Nafion ionomer was applied to the CAL by spraying on its surface and a gradient of Nafion ionomer loading was created in the CAL. Even if the technique used in this work to make a cathode is different from our previous work and a uniform ionic conductivity distribution in the cathode CAL is expected here, we would like to believe that an optimal amount of Nafion ionomer loading in a PEMFC cathode CAL is always true. The improvement of cathode performance with an increase in D_{eff}/R_a^2 can be explained by the decrease of the time constant for O_2 diffusion inside a flooded agglomerate particle. The possibility of observing the change of Tafel slope from a normal value to a double value associated with liquid-phase O_2 diffusion process on a polarization curve of a PEMFC cathode was discussed extensively in the literature.[3,9] Interestingly, the change of Tafel slope was also observed in the kinetic studies of the catalyst Pt on a rotating disk electrode:[14-18] at high potentials a single Tafel slope is exhibited, and at low potentials a double Tafel slope is exhibited. The change of Tafel slope observed in the kinetic studies was explained by the change of O_2 reduction mechanism from a four-electron path to a two-electron path.[14,15]

To demonstrate how effectively our numerical algorithm is improved by calculating the model equations and each set of sensitivity equations separately and by providing a banded Jacobian matrix, the computer time required to solve our nonlinear model equations with the change of their Jacobian matrix structure is summarized in Table III. Because there are only two equations in our model for each spatial node point, the calculation of 200 equations indicates our use of 100 node points to discretize the spatial coordinate z. By solving 200 equations six times (only one current density data point is considered), we want to simulate the total computer time required to solve the model equations and each set of sensitivity equations separately. By solving 1200 equations once, we want to simulate the computer time necessary for solving the coupled model and sensitivity equations at the same time. Table III shows that the numerical efficiency associated with the separate calculation of model equations and each set of sensitivity equations is only improved by 20% if a sparse Jacobian matrix exists and it is provided. For the case that there exists a sparse Jacobian matrix but it is not provided, the numerical efficiency is improved 70%. For the case that there exists a dense Jacobian matrix and it is not provided, the separate calculation improves the numerical efficiency by 83%. Because an improvement of numerical efficiency associated with the separate calculation is always true, this method should be recommended in a nonlinear parameter estimation problem involving the numerical solution of differential equations.

Conclusions

The simultaneous fit of three experimental curves was performed successfully by using a nonlinear parameter estimation method and an optimized numerical algorithm. The joint confidence region obtained for the five parameters of interest are found to be more appropriate for the determination of their true parameter values rather than the confidence intervals. The values of parameters obtained in this work indicate that ionic conduction and gas-phase transport are two processes influencing the performance of a PEMFC air cathode significantly. While ionic conduction influences the cathode performance over a wide range of current densities, gas-phase transport influences the cathode performance only at high current densities.

Acknowledgments

The authors are grateful for financial support of the project for Hybrid Advanced Power Sources by the National Reconnaissance Office (NRO) under contract no. NRO-000-01-C-4368.

The University of South Carolina assisted in meeting the publication costs of this article.

List of Symbols

b	normal Tafel slope, V
c_G	total gas concentration, mol/cm^3
c_{ref}	reference liquid phase O_2 concentration, mol/cm^3
D_{eff}	effective diffusion coefficient of O_2 in a flooded agglomerate particle, cm^2/s
D^0_{ON}	binary diffusion coefficient of O_2 and N_2 in a free gas stream, cm^2/s
D^0_{OW}	binary diffusion coefficient of O_2 and water vapor in a free gas stream, cm^2/s
D^0_{NW}	binary diffusion coefficient of N_2 and water vapor in a free gas stream, cm^2/s
E	equilibrium potential of a cathode relative to a standard H_2 reference electrode, V
E^0_O	standard potential of a cathode relative to a standard H_2 reference electrode, V
F	Faraday's constant, 96,487 C/equiv.
F	F distribution
H	Henry's constant, [mol/cm^3(l)]/[mol/cm^3(g)]
I	steady-state operating current density, A/cm^2
$\mathbf{I}$	identity matrix
i_{ref}	exchange current density of the O_2 reduction reaction evaluated a reference O_2 concentration of 1.0×10^{-6} mol/cm^3 in a flooded agglomerate particle, A/cm^3
$\mathbf{J}$	the matrix of the partial derivatives of the dependent variable with respect to estimation parameters evaluated at all the experimental data point.
j_O	steady-state generation rate of O_2 gas per unit volume of the cathode CAL, mol/cm^3
l_B	thickness of the GDL, cm
l_c	thickness of the CAL, cm
P	total gas pressure, atm
R	universal gas constant, 8.3143 J/mol/K
$\mathbf{R}$	correlation matrix
R_a	radius of an agglomerate particle, cm
S^2	squared residual
S_E	the standard deviation
S_{x,θ_j}	sensitivity coefficient, $\partial x/\partial\theta_j$
S_{η,θ_j}	sensitivity coefficient, $\partial\eta/\partial\theta_j$
t	student's t distribution
T	absolute temperature, K
x	steady-state mole fraction of O_2 in the gas pores
z	normalized spatial coordinate in either the GDL or CAL, $0 \leqslant z \leqslant 1$
w	mole fraction of water vapor in the gas pores

Greek

$\boldsymbol{\theta}$	parameter vector to be estimated

θ_j^* point estimate of parameter θ_j
η steady-state overpotential, V
φ_B volume fraction of gas pores in the GDL
φ_c volume fraction of gas pores in the CAL
κ_{eff} effective ionic conductivity of the electrolyte, S/cm
Φ_1 steady-state cathode potential, V
Φ_1^* experimental steady-state cathode potential, V

Subscripts

B GDL
c CAL
T Transpose
−1 Inverse

References

1. T. E. Springer, M. S. Wilson, and S. Gottesfeld, *J. Electrochem. Soc.*, **140**, 3513 (1993).
2. M. Maja, P. Tosco, and M. Vanni, *J. Electrochem. Soc.*, **148**, A1368 (2001).
3. F. Jaouen, G. Lindberg, and G. Sundholm, *J. Electrochem. Soc.*, **149**, A437 (2002).
4. D. M. Bernardi and M. W. Verbrugge, *J. Electrochem. Soc.*, **139**, 2477 (1992).
5. L. Pisani, G. Murgia, M. Valentini, and B. D'Aguanno, *J. Electrochem. Soc.*, **149**, A898 (2002).
6. T. E. Springer, in *Tutorials in Electrochemical Engineering*, R. F. Savinell, J. M. Fenton, A. West, S. L. Scanlon, and J. W. Weidner, Editors, Vol. 99-14, p. 208, The Electrochemical Society Proceedings Series, Pennington, NJ (1999).
7. T. E. Springer, T. A. Zawodzinski, M. S. Wilson, and S. Gottesfeld, *J. Electrochem. Soc.*, **143**, 587 (1996).
8. Q. Guo and R. E. White, *J. Electrochem. Soc.*, **151**, E133 (2004).
9. M. L. Perry, J. Newman, and E. J. Cairns, *J. Electrochem. Soc.*, **145**, 5 (1998).
10. J. Ihonen, F. Jaouen, G. Lindbergh, A. Lundblad, and G. Sundholm, *J. Electrochem. Soc.*, **149**, A448 (2002).
11. A. Pebler, *J. Electrochem. Soc.*, **133**, 9 (1986).
12. A. Constantinides and N. Mostoufi, *Numerical Methods for Chemical Engineers with MATLAB Applications*, pp. 439-481, Prentice Hall, Upper Saddle River, NJ (1999).
13. Y. Bard, *Nonlinear Parameter Estimation*, p. 227, Academic Press, New York (1974).
14. U. A. Paulus, T. J. Schmidt, H. A. Gasteiger, and R. J. Behm, *J. Electroanal. Chem.*, **495**, 134 (2001).
15. C. F. Zinola, A. M. Castro Luna, and A. J. Arvia, *Electrochim. Acta*, **13**, 1951 (1994).
16. S. Mukerjee, S. Srinivasan, and M. P. Soriaga, *J. Phys. Chem.*, **99**, 4577 (1995).
17. A. Parthasarathy, S. Srinivasan, and A. J. Appleby, *J. Electrochem. Soc.*, **139**, 2530 (1992).
18. J. Shan and P. G. Pickup, *Electrochim. Acta* **46**, 119 (2000).
19. M. S. Wilson, U.S. Pat. 5,211,984 (1993).
20. E. L. Clussler, *Diffusion Mass Transfer in Fluid Systems*, 2nd ed. p. 103, Cambridge University Press, New York (1997).
21. T. V. Nguyen, J. Mitchell, and W. He, in *Symposium on Fuel Processing and Fuel Cells*, AIChE 2001 Annual Meeting, Paper No. 4, Reno, Nevada (2001).
22. W. He and T. Nguyen, Paper 130 presented at The Electrochemical Society Meeting, Philadelphia, PA, May 12-17, 2002.
23. W. He, G. Lin, and T. V. Nguyen, *AIChE J.*, **49**, 3221 (2003).
24. T. I. Evans and R. E. White, *J. Electrochem. Soc.* **136**, 2798 (1989).
25. L. Genies, R. Faure, and R. Durand, *Electrochim. Acta* **44**, 1317 (1998).
26. Q. Guo, M. Cayetano, Y. Tsou, E. S. De Castro, and R. E. White, *J. Electrochem. Soc.* **150**, A1440 (2003).